This is a repository copy of *Characterising eclipsing white dwarf M dwarf binaries from multi-band eclipse photometry*.

White Rose Research Online URL for this paper:
https://eprints.whiterose.ac.uk/185902/

Version: Accepted Version

This is a pre-copyedited, author-produced PDF of an article accepted for publication in Monthly Notices of the Royal Astronomical Society following peer review. The version of record Alex J Brown, Steven G Parsons, Stuart P Littlefair, James F Wild, R P Ashley, E Breedt, V S Dhillon, M J Dyer, M J Green, P Kerry, T R Marsh, I Pelisoli, D I Sahman, Characterising eclipsing white dwarf M dwarf binaries from multi-band eclipse photometry, Monthly Notices of the Royal Astronomical Society, 2022;, stac1047 is available online at: https://doi.org/10.1093/mnras/stac1047.

Characterising eclipsing white dwarf M dwarf binaries from multi-band eclipse photometry

Alex J. Brown,[1]* Steven G. Parsons,[1] Stuart P. Littlefair[1] James F. Wild,[1] R. P. Ashley,[2] E. Breedt,[3] V. S. Dhillon,[1,4] M. J. Dyer,[1] M. J. Green,[5] P. Kerry,[1] T. R. Marsh,[6] I. Pelisoli,[6] D. I. Sahman,[1]

[1]*Department of Physics and Astronomy, Hicks Building, The University of Sheffield, Sheffield, S3 7RH, UK*
[2]*Isaac Newton Group of Telescopes, Apartado de Correos 321, Santa Cruz de La Palma, E-38700, Spain*
[3]*Institute of Astronomy, University of Cambridge, Madingley Road, Cambridge CB3 0HA, UK*
[4] *Instituto de Astrofisica de Canarias, E38205 La Laguna, Tenerife, Spain*
[5]*Department of Astrophysics, School of Physics and Astronomy, Tel Aviv University, Tel Aviv 6997801, Israel*
[6]*Department of Physics, University of Warwick, Gibbet Hill Road, Coventry, CV4 7AL, UK*

ABSTRACT

With the prevalence of wide-field, time-domain photometric sky surveys, the number of eclipsing white dwarf systems being discovered is increasing dramatically. An efficient method to follow these up will be key to determining any population trends and finding any particularly interesting examples. We demonstrate that multi-band eclipse photometry of binaries containing a white dwarf and an M dwarf can be used to determine the masses and temperatures of the white dwarfs to better than 5 per cent. For the M dwarfs we measure their parameters to a precision of better than 6 per cent with the uncertainty dominated by the intrinsic scatter of the M dwarf mass-radius relationship. This precision is better than what can typically be achieved with low-resolution spectroscopy. The nature of this method means that it will be applicable to LSST data in the future, enabling direct characterisation without follow-up spectroscopy. Additionally, we characterise three new post-common-envelope binaries from their eclipse photometry, finding two systems containing hot helium-core white dwarfs with low-mass companions (one near the brown dwarf transition regime) and a possible detached cataclysmic variable at the lower edge of the period gap.

Key words: (stars:) binaries: eclipsing – (stars:) white dwarfs – stars: late-type – techniques: photometric

1 INTRODUCTION

The majority of stars within binaries will evolve as if they were single stars, never interacting with their companion other than gravitationally. Around 25 per cent, however, are born sufficiently close that at some point during their lives they will interact, transferring material between them and potentially affecting their future evolution (Willems & Kolb 2004). Many of these close binary systems will undergo a phase in their lifetimes known as common-envelope evolution, where both stars orbit within a shared envelope of material drawn from the expanding outer layers of the more evolved star. Drag forces between the common-envelope and the two stars cause them to spiral in to shorter orbital periods. Assuming the binary doesn't merge during this phase, the immediate product will be a short period post-common-envelope binary (PCEB), usually containing a low-mass main sequence star – otherwise known as an M dwarf – and the remnant core of the more evolved star which will become a white dwarf (WD).

As well as being a key tracer of the relatively poorly understood common-envelope phase, these white dwarf main sequence (WDMS) binaries are thought to be the progenitors to a wide variety of interesting and exotic astrophysical phenomena, from cataclysmic variables (CVs) and hot subdwarf stars (Han et al. 2002) to the fu-

ture gravitational-wave source double WDs and the cosmologically-important Type Ia supernovae.

Additionally, the compact nature of these WDMS binaries – specifically those with lower mass companions and referred to hereafter as WD+M dwarf (WDdM) binaries – means a relatively large proportion are seen to eclipse, allowing for the determination of precise constraints on the physical parameters of the system (Parsons et al. 2017, 2018). They are therefore ideal systems with which to test models of stellar physics as well as providing much-needed insight into the common-envelope phase itself (Zorotovic et al. 2010; Toonen & Nelemans 2013). At the last published count, the sample of eclipsing WDdM PCEBs stood at around 80 systems (Parsons et al. 2015). With large-scale photometric sky surveys such as the Zwicky Transient Facility (ZTF) (Bellm et al. 2019; Graham et al. 2019), and Legacy Survey of Space and Time (LSST) (Ivezić et al. 2019) in the future, this number is set to increase considerably (with more than 200 systems already found in ZTF, Van Roestel 2019). With fainter systems being discovered, this will make efficient and reliable follow-up and characterisation of these systems more difficult. Previously, follow-up observations of newly discovered WDdM systems have typically relied on low-resolution spectroscopy to determine initial system parameters, attempting to fit the Balmer sequence of the WD as well as the spectral energy distributions (SEDs) of both components (Rebassa-Mansergas et al. 2007, 2010, 2013, 2016). This is complicated by the dilution of spectral features due to the com-

panion star which makes disentangling the two component spectra difficult and is hard to apply to the increasing population of fainter systems. Purely photometric approaches have been used recently e.g. Rebassa-Mansergas et al. (2021) who derived parameters for WDdM binaries using the Virtual Observatory SED Analyser to fit two component models to the SEDs and parallaxes of the systems. While this is a useful method, especially for large samples, it remains relatively untested and the uncertainties are difficult to estimate. It is also unclear how the fitted parameters are affected by any phase dependence on the photometry such as reflection effect or ellipsoidal modulation, especially given that the photometric measurements taken across the different bands are unlikely to be taken at similar orbital phases.

For eclipsing systems in particular, the shape of the eclipse light curve provides powerful constraints on the system parameters. However, this has not yet been exploited for initial parameter estimation, instead being used in conjunction with radial velocity measurements to retrieve precise model-independent parameters for detailed studies (Parsons et al. 2010, 2017, 2018). Given that a primary eclipse (the eclipse of the WD by the M dwarf companion) light curve will require a similar amount of telescope time as a low-resolution identification (ID) spectrum, there is potential to use eclipse photometry for initial follow-up instead of low-resolution spectroscopy. There are many benefits to this, one of which being that photometry can be used with fainter systems than spectroscopy can manage. This will become a major advantage as many of the systems discovered by LSST will be so faint that eclipse photometry will be the only viable route to measuring their parameters. Other benefits originate from the clean separation of the two stars, permitted by the eclipse of the WD. This removes the issue of disentangling the two component spectra that spectroscopy suffers from and allows for robust fitting of both stars even when one is much brighter than the other, especially useful for discerning systems with faint brown dwarf companions or small, high-mass WDs. Additional advantages come from the high temporal resolution of an eclipse light curve, allowing for detection of short-term variability which may indicate the presence of a WD that is pulsating or magnetic. These specific WDdM subtypes are of particular interest and would likely be missed by spectroscopy. Moreover, should an interesting system be discovered, eclipse light curve data can then be reused in combination with radial velocity measurements for more detailed study whereas low-resolution spectroscopy is much less useful beyond the initial parameter estimation.

Here, we present a Markov Chain Monte Carlo (MCMC) code[1] developed to make use of these advantages to fit the parameters of these systems, namely the masses and temperatures of the WD and M dwarf components (referred to as the primary and secondary respectively), using only high-cadence multi-band photometry of the primary eclipse in combination with *Gaia* parallax measurements (Gaia Collaboration et al. 2016, 2021) and theoretical models. We aim to do this more accurately and reliably than low-resolution spectroscopy and with sufficient precision to discern systems of particular interest. Specifically, we aim to determine the WD parameters to better than 5 per cent which is sufficient to discern interesting WD subtypes such as ZZ Ceti. For the M dwarfs, we aim for a similar level of precision which is adequate for distinguishing companions at, or close to, the substellar boundary. In terms of accuracy, the goal is for the parameters of both components to be within, at most, three standard deviations of the 'true' values. Here we assume the high-precision model-independent values (Parsons et al. 2017, 2018) to represent these 'true' parameters.

2 ECLIPSE MODELLING

We construct a multi-wavelength light curve model using the `lcurve` code (see Copperwheat et al. 2010, appendix A) to model the light curves of WDdM binaries immediately around the primary eclipse. The eclipse provides the strongest constraints on the system parameters and is sufficient to characterise the system without needing to observe a full orbit. Using this small region around the eclipse has the benefit of being much more efficient in terms of telescope time as well as being much faster to fit (due to a significant reduction in the number of light curve points that have to be modelled).

An `lcurve` eclipse model for a detached binary is defined by 19 parameters:

(i) The mass ratio, $q = \frac{M_2}{M_1}$.

(ii) The radii, R, of each star scaled by the orbital separation, a, $\frac{R}{a}$. These radii are measured from the centre of mass of the star towards the inner Lagrangian point, L_1.

(iii) The orbital inclination, i.

(iv) The equivalent blackbody temperature, T_{BB}, of each star. These blackbody temperatures, together with the effective wavelength, λ_{eff}, of the model define the monochromatic flux normal to the surface of the star via the Planck law.

(v) The orbital ephemeris of the system, defined by the orbital period, P, and the time of mid-eclipse, T_0.

(vi) The limb-darkening coefficients of both stars, c_1, c_2, c_3, and c_4, using the four-parameter prescription (Claret 2000).

(vii) The bandpass-specific gravity-darkening coefficient for the secondary star, y.

(viii) The fraction of incident flux from the WD that is absorbed by the M dwarf, F_{abs}.

Many of these parameters vary with wavelength, most of which have little effect on the eclipse profile, resulting in an impractical number of free parameters when fitting multiple bands simultaneously. Additionally, degeneracies exist between some of these parameters, most notably the two scaled radii and the orbital inclination (Parsons et al. 2017). Theoretical models and relations are therefore required in order to define these parameters from those that we are interested in – the WD masses and effective temperatures and the masses of their M dwarf companions – during the fitting procedure. In the following sections we outline how this is achieved.

2.1 Mass-radius relations

The shape of the WD eclipse primarily constrains the scaled radii of the two stars and their orbital inclination. In order to retrieve masses from the eclipse photometry and break the degeneracy between scaled radii and inclination, mass-radius relations for both stars are required.

For the WD we use the mass-radius relations of Panei et al. (2007), Fontaine et al. (2001), and Althaus et al. (2005) for He-, CO-, and ONe-core compositions respectively; This core composition must be selected for a particular fit.[2] Mass-radius relations for low- and intermediate-mass WDs have been well tested observationally and shown to be robust and accurate to within a couple of per cent (Parsons et al. 2017). For higher mass WDs, the models are assumed

---

[1] https://github.com/Alex-J-Brown/pylcurve

[2] For systems with best-fit WD masses close to a border between core compositions it is worth running the fit again with the alternative core composition in order to determine which is most consistent with the expected mass range for the respective core composition (i.e. a 0.3 $M_\odot$ CO-core WD is unlikely).

to be similarly reliable, however, should this not be the case they will at least be sufficient to mark the system as containing a high mass WD worthy of further study. In terms of the outer hydrogen layer mass, models with thick hydrogen layers ($M_{\rm H}/M_{\rm WD} = 10^{-4}$) have been shown to represent WDs in PCEBs well in the majority of measured cases (Parsons et al. 2017). We therefore use these thick layer models for our WD mass-radius relations.

M dwarfs, however, are often found to be inflated relative to theoretical models for their mass, with radii typically found to be around 5 to 15 percent larger than models predict (López-Morales & Ribas 2005; López-Morales 2007; Parsons et al. 2018; Kesseli et al. 2018). In an attempt to minimise any systematic effects arising from inflation, we produce a semi-empirical mass-radius relation for M dwarfs. We assign masses to a sample of 15 279 M dwarfs with *Gaia* parallaxes, radii, and 2MASS K_S measurements (Morrell & Naylor 2019) using the preferred fifth order ($n = 5$) polynomial representation of the $K_{\rm abs}-M_*$ relation (Mann et al. 2019). The resulting M dwarf mass-radius relationship is shown in Figure 1. A population of stars exist above the main group. Checking these against the rest of the sample it is clear that they lie above the *Gaia* main sequence and are likely binaries or pre-main-sequence stars, explaining their anomalous radii measurements. Cross-matching these outlying points with Simbad confirms that a large proportion of these are indeed pre-main-sequence stars, variables, or binaries and can be discarded. We use an iterative sigma-clipping fitting procedure using a fifth-order polynomial to discard these points, removing ≈ 3 per cent of the total sample. We then follow this up with an MCMC fit to retrieve the final relation (Table 1) while providing reliable uncertainty estimates on the polynomial coefficients. Due to the sparse nature of the sample in the low mass range and the convergence with the theoretical tracks of Baraffe et al. (2015), we switch to using the theoretical models below the mass where the semi-empirical fit crosses the models. This occurs at $M_* = 0.121\,M_\odot$. We use the 1 Gyr model from Baraffe et al. (2015) below this point. We note that the apparent upturn in the sample above $\approx 0.65\,M_\odot$ is not real and is a result of the fitted effective temperatures in the M dwarf sample being limited to below 4400 K and therefore stars with slightly higher temperatures than this will require a larger radius to fit their observed luminosity. We therefore only consider the fitted relation valid below this point.

There is some scatter in the M dwarf sample around the best-fit semi-empirical relation. Much of this scatter is likely genuine variation in the radii of M dwarfs with similar masses. This has been seen before with Parsons et al. (2018) measuring a scatter of ≈ 5 per cent in the radii of M dwarfs in their sample. Additionally, some may be due to scatter in the fitted temperature for a given K_S magnitude. This is demonstrated by the gap in the sample due to the discontinuity in models at $T_{\rm eff} = 4000\,K$, described by Morrell & Naylor (2019), and which therefore describes a line of constant temperature. Additional contributions to the scatter come from K_S magnitude uncertainties (typically below 2 per cent) and metallicity dependence (estimated to be ≈ 1.7 per cent, Morrell & Naylor 2019).

The fractional residuals have a standard deviation of ≈ 3 per cent. This is slightly higher when measuring the scatter as a function of radius with fractional residuals of ≈ 3.5 per cent. This means that a fit with a hypothetical perfect determination of the secondary radius would translate into a secondary mass distribution with a standard deviation of 3.5 per cent and is therefore the maximum precision possible on the secondary mass using this relation. Additional errors in this mass-radius relation may be introduced through the $K_{\rm abs}-M_*$ relation used to derive it, with Mann et al. (2019) predicting that it is able to determine the mass of a star to a precision of ≈ 2 per cent. They also mention that there exists a small ($\lesssim 2$ per cent) systematic
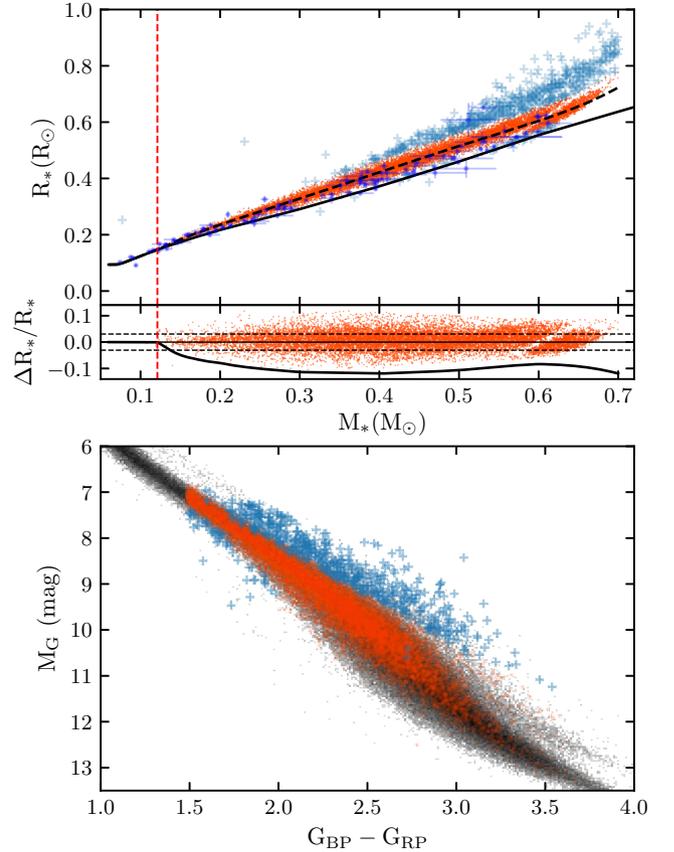
Figure 1. above) Semi-empirical M dwarf mass-radius relation (black dashed line). Red points are those that remain after the sigma clipping while the light blue crosses are those that are discarded which are mainly pre-main-sequence stars or unresolved binaries. Dark blue points with error bars are M dwarfs with well constrained masses and radii collated in Parsons et al. (2018, table A1). The solid black line shows the 1 Gyr track of Baraffe et al. (2015). Fractional residuals relative to the semi-empirical relation are shown below with the dashed lines indicating $\pm 1\sigma$. The transition between the fitted relation and the Baraffe 1 Gyr model is indicated by the vertical dashed line. The gap in the data around $M_* = 0.6\,M_\odot$ is due to the discontinuity mentioned by Morrell & Naylor (2019) at $T_{\rm eff} = 4000\,K$. **below**) *Gaia* Hertzsprung-Russell diagram for stars within 100 pc with the M dwarf mass-radius sample overplotted in red. Blue crosses show those discarded by the sigma-clipping procedure demonstrating that they mostly lie above the main sequence.

offset for literature M dwarfs in eclipsing binary systems as compared to their predictions from the relation, possibly due to magnetic activity or rotation rates. Summing these contributions in quadrature with the 3.5 per cent scatter gives an estimated maximum precision in the secondary mass of ≈ 5 per cent. Any additional systematic contributions due to binarity (i.e. magnetic activity, rotation effects, or Roche distortion) are difficult to examine and we assume them to be small.

While this estimated uncertainty is straightforward to fold into the MCMC fitting routine, it increases the MCMC convergence time considerably, making it prohibitively long. We therefore choose to assume the best fit semi-empirical relation and account for the additional uncertainty in the relations at the end of the fitting, combining the formal errors from the MCMC in quadrature with the 5 per cent uncertainty for the secondary mass, and a 1 per cent uncertainty for

	a_5	a_4	a_3	a_2	a_1	a_0
μ	27.4	−54.1	41.1	−14.9	3.53	−0.124
σ	1.8	3.6	2.7	0.9	0.16	0.010

Table 1. Best-fit coefficients and uncertainties for a fifth-order polynomial fit to the semi-empirical M dwarf mass and radius measurements of the form $\frac{R}{R_\odot} = \sum_{n=0}^{5} a_n \left(\frac{M}{M_\odot}\right)^n$.

the primary mass (as WD mass-radius relations have not yet been tested to higher precision than this).

2.2 Irradiation

Many of these WDdM binaries contain hot WDs ($T_{\rm eff} > 20\,000$ K). Given the small orbital separations in PCEBs this can result in high irradiating fluxes incident on the surface of the M dwarf, often many times greater than the typical outgoing flux from the secondary. This high irradiation can induce an inflation in the M dwarf companion by effectively blocking outgoing flux over a portion of the star's surface area and therefore requiring a larger unirradiated surface (at most ≈ 7 per cent larger, Ritter et al. 2000) in order to expel the excess luminosity and retain thermal equilibrium. We attempt to include this effect in our model using a simplified method where we assume that the effective temperature over the full surface of the secondary is uniform. We calculate the effective surface area, $s_{\rm eff}$, over which the outgoing flux is blocked (Ritter et al. 2000, equation 60) which can then be used to determine the inflated radius, $R_{\rm irr}$, using

$$R_{\rm irr} = R_0 (1 - s_{\rm eff})^{-0.1} \tag{1}$$

where R_0 is the radius of the secondary without irradiation (i.e. the output from the semi-empirical mass-radius relation).

2.3 Roche distortion

The radii referred to in the previous sections are of an isolated and therefore spherically symmetric star. The compact nature of PCEBs mean that the Roche distortion of the secondary due to the WD can become significant and therefore needs to be corrected for. To do this we assume that the radius of a spherically symmetric star, used above, is equivalent to the volume averaged radius of the star when experiencing Roche distortion. There is no analytical equation for calculating this correction. We therefore produce tables relating the scaled radius measured towards L_1, as used by lcurve, to the scaled radius of a spherically symmetric star with the equivalent volume as a function of binary mass ratio. For a given mass ratio the scaled radius towards L_1 defines a Roche equipotential representing the surface of the star. We then determine the positions of points on this equipotential surface over a range of latitudes and longitudes and compute the volume of the convex hull defined by these points. The volume-averaged scaled radius can then be easily determined. The conversion then becomes a simple interpolation given the binary mass ratio and the volume-averaged scaled radius.

2.4 Blackbody temperatures

As previously mentioned, the temperatures used by lcurve are a substitute for the monochromatic specific intensity normal to the surface of the star, i.e. at $\mu = \cos\theta = 1$ where θ is the angle between the line normal to the stellar surface and the line of sight. Claret et al. (2020) provide tables of specific intensities at $\mu = 1$, together with limb-darkening coefficients, c_k, for WDs in both the

SDSS (Fukugita et al. 1996) and Super-SDSS (Dhillon et al. 2021) photometric systems.

For main sequence stars, no such tables exist for the Super-SDSS system. We therefore use the PHOENIX specific intensity model spectra from the Göttingen Spectral Library (Husser et al. 2013) to compute these. We calculate synthetic fluxes, $\langle f_\lambda \rangle_x$, in the Super-SDSS system according to

$$\langle f_\lambda \rangle_x = \frac{\int f_\lambda(\lambda) S_x(\lambda) \lambda d\lambda}{\int S_x(\lambda) \lambda d\lambda}, \tag{2}$$

where $f_\lambda(\lambda)$ is the spectral flux density as a function of wavelength, λ, and $S_x(\lambda)$ is the throughput of the chosen filter. We do this at each value of μ supplied by the PHOENIX spectra. These can then be normalised to the flux at $\mu = 1$ and fit with the four-parameter law of Claret (2000),

$$\frac{I_\lambda(\mu)}{I_\lambda(1)} = 1 - \sum_{k=1}^{4} c_k (1 - \mu^{\frac{k}{2}}), \tag{3}$$

where $I_\lambda(\mu)$ is the specific intensity relative to that at $\mu = 1$. Rather than use the synthetic fluxes at $\mu = 1$ to determine the lcurve temperatures, we calculate the total synthetic flux of the star, F_λ, according to our best-fit limb-darkening law using

$$F_\lambda = 2\pi \int_0^1 I_\lambda(\mu) \mu d\mu. \tag{4}$$

We then take the central intensity required to match the total synthetic flux with the synthetic flux calculated for the equivalent HiRes PHOENIX spectrum. This ensures the absolute flux of a star modelled with these limb darkening parameters remains consistent with the full disk PHOENIX model.

Temperatures of blackbody spectra that give monochromatic specific intensities equal to these specific intensities at $\mu = 1$ are then computed at the pivot wavelength of each filter in the SDSS and Super-SDSS systems.

2.5 Model summary

In summary, multi-band eclipse light curves clearly resolve the SEDs[3] of both components, with the depths of the eclipses showing the flux contributed by the WD and the in-eclipse flux showing the contribution from the secondary. These SEDs from the eclipse light curves constrain the effective temperatures of both stars which, together with parallax information, places constraints on their radii. The shape of the eclipse strengthens this constraint whilst also restricting the orbital separation and therefore the masses of the stars when combined with mass-radius relations.

We use lcurve to model these light curves, defining our lcurve model from the parameters of interest – T_1, T_2, M_1, M_2, i, T_0, ϖ, and $E(B - V)$, where ϖ is the parallax – together with the orbital period, P, and the bandpass of the observation, via various theoretical models and relations. The lcurve parameters, described previously, are defined as follows:

(i) The mass ratio, q, is set from the masses as $\frac{M_2}{M_1}$.

---

[3] When referring to the method described in this work, the SED is from the eclipse light curves alone and does not include any additional photometric data

(ii) The scaled radius of the primary, $\frac{R_1}{a}$, is defined by the WD mass-radius relation for the chosen core composition together with Kepler's third law and therefore depends on the WD mass and temperature, the secondary mass, and the orbital period. The scaled radius of the secondary, $\frac{R_2}{a}$, is primarily defined by the semi-empirical mass-radius relation together with Kepler's third law, with corrections for irradiation and Roche distortion. It is therefore dependent on the WD mass and temperature, the secondary mass and temperature, and the orbital period of the system.

(iii) The orbital inclination, i, is a free parameter.

(iv) The equivalent blackbody temperatures of each star, T_{BB}, is defined by the mass and temperature of the respective star together with the chosen bandpass.

(v) For the orbital ephemeris, T_0 is a free parameter in the fit while P is fixed at a previously determined value.

(vi) The limb-darkening coefficients of both stars, c_1, c_2, c_3, and c_4, like the blackbody temperatures, are defined by the mass and temperature of the respective star together with the chosen bandpass.

(vii) The gravity-darkening coefficient for the secondary star, y, is also defined by its mass and temperature along with the chosen bandpass.

(viii) The fraction of incident flux from the primary that is absorbed by the secondary can generally be ignored due to only fitting a small region surrounding the primary eclipse. We therefore leave it fixed at $F_{abs} = 0.5$.

2.6 χ^2 calculation for flux calibrated light curves

When generating a model light curve, `lcurve` can be supplied with a scale factor which sets the absolute flux level of the light curve. It is therefore possible to calculate the scale factor required to produce a true flux light curve model from the parallax, interstellar extinction, and orbital separation. The issue with this approach is that any small error in the flux calibration of the data will cause issues with the fitting. This is because the flux calibrated eclipse light curves are unlikely to correspond exactly to the model SEDs of both stars, resulting in the fit being unable to correctly model both the in-eclipse and out-of-eclipse flux simultaneously, preventing an accurate fit to the eclipse shape and therefore reliable parameter estimation. We instead allow `lcurve` to automatically scale the model to the data, calculating the χ^2 using this scaled model.

To include the absolute flux information, we take the WD flux contribution output by `lcurve` for the scaled model (a reliable measure of the depth of the primary eclipse) and compare this to the theoretical WD flux for the given temperature, mass, parallax, and extinction, calculating the χ^2 for this using the flux calibration uncertainty. This method allows for a more proper handling of the uncertainties, treating those from the flux calibration and from the differential photometry independently. We combine these two values of χ^2, repeating this over all observed bands to obtain an overall χ^2 value for the full flux calibrated model.

2.7 Fitting procedure

To fit the light curves of a system we use MCMC, implemented through the `emcee` Python package (Foreman-Mackey et al. 2013). For each walker position an `lcurve` light curve model is generated for each observed bandpass with the log probability calculated as described in Section 2.6. The log probability from this model is combined with a parallax prior. We use a bounded Gaussian prior with a mean and standard deviation corresponding to the *Gaia* `parallax`

and `parallax_error` (Gaia Collaboration et al. 2021) respectively with a limit at two standard deviations above and below.

The use of the *Gaia* parallax distribution as a prior in the MCMC prevents systematic issues that would be introduced by using the distance. All systems considered in this work have a `parallax_over_error` > 10 and, when combined with the photometric information, will be constrained sufficiently that the inclusion of the galactic stellar density distribution is unnecessary.

For systems with larger uncertainty in their parallax measurement, or maybe even no parallax information at all as will be the case for many of the systems discovered by LSST, this method can still be successful in fitting the parameters. It is possible, however, that in the case of systems where the SED of either star does not match the models well (most likely due to irradiation effects or star spots on the secondary), that the fit will compensate using the parallax. For systems with good parallax measurements, this effect is relatively obvious and can be flagged. Assuming it is the secondary SED that is causing the problem (which is most likely) then allowing its temperature to be independent in each band can allow the fit to converge to values consistent with the measured parallax[4]. For those with high parallax uncertainties, though, it may go unnoticed, leading to incorrect parameters.

Priors on all other parameters are uniform with upper and lower limits defined by the range of the model grids. Each MCMC chain is run with 100 walkers for 20 000 steps. The chains are then inspected and a number of steps are discarded from the beginning as burn-in. The number of steps discarded is chosen to remove any steps before the final equilibrium position.

3 OBSERVATIONS

In order to validate this modelling, we test our fitting code on three previously well characterised WDdM PCEBs. We use archival photometry of these systems from ULTRACAM (Dhillon et al. 2007) and HiPERCAM (Dhillon et al. 2021) to test that the method is successful when using either three-band or five-band data. We then fit three, previously unpublished, systems, all observed with ULTRACAM (all observations detailed in Table 2)

3.1 Reduction

We used the HiPERCAM pipeline (Dhillon et al. 2021) to debias, flat-field correct – and defringe in the case of HiPERCAM z_s data – and then extract aperture photometry. We allowed the radius of the target aperture to vary in line with the measured full-width at half-maximum of a reference star in each frame to minimise the effects of seeing variation. The counts from the target were measured relative to a brighter comparison star to remove any transparency variations and atmospheric extinction effects.

3.2 Flux calibration

Using the SED of the WD to determine its temperature requires precise flux calibration. This requirement is emphasised by the significant temperature dependence of the WD mass-radius relations

---

[4] Note that this increases the number of dimensions for the MCMC and so increases the convergence time as well as removing the effective temperature information for the secondary. It is therefore best left as a backup method in the case where the original fit is struggling.

Target	Date	UT start	Filters	Telescope-Instrument	Exp time (s)	Sky transparency	FWHM (")
NN Ser	2019-07-09	23:39:06	$u_s g_s r_s i_s z_s$	GTC-HiPERCAM	1.0	Some dust but stable	1.5
SDSS J0838+1914	2010-12-13	07:41:55	$u'g'r'$	NTT-ULTRACAM	4.8	Photometric	2
SDSS J1028+0931	2018-01-30	06:07:53	$u_s g_s r_s$	NTT-ULTRACAM	2.5	Photometric	1
2MASS J1358−3556	2018-06-01	03:04:59	$u_s g_s i_s$	NTT-ULTRACAM	4.0	Photometric	1.5
EC 12250−3026	2018-05-31	23:03:24	$u_s g_s i_s$	NTT-ULTRACAM	3.0	Photometric	1.5
SDSS J1642+0135	2019-03-04	07:40:28	$u_s g_s i_s$	NTT-ULTRACAM	5.0	Photometric	1.5

Table 2. Journal of observations.

on which this method relies heavily. Flux calibration is complicated by the significant departure of the HiPERCAM and ULTRACAM Super-SDSS filter sets from the standard SDSS system. This departure is most notable in the u_s band where it can be tenths of magnitudes. The typical solution would be to observe a selection of spectro-photometric standard stars with well known spectra – observed or theoretical – spanning the full wavelength range of the filter set in order to calibrate the observed light curves from synthetic photometry. This is the method that will be employed in future works using the *Gaia* spectro-photometric standard stars (Pancino et al. 2012; Altavilla et al. 2015; Marinoni et al. 2016; Altavilla et al. 2021; Pancino et al. 2021). Synthetic AB magnitudes of these *Gaia* spectro-photometric standard stars computed for the ULTRACAM and HiPERCAM Super-SDSS systems are included in appendix A for future reference along with a more thorough analysis of the differences between the Super-SDSS and SDSS photometric systems.

However, as this work is based on archival photometry, only flux standards with USNO–40 photometry (Smith et al. 2002) are available for flux calibration. We instead fit PHOENIX model spectra to the USNO–40 and *Gaia* photometry of these standards to calculate the magnitude offsets required to transform the USNO–40 photometry into the Super-SDSS system.

Using an MCMC method, implemented through the `emcee` Python package, we fit the effective temperature, surface gravity, radius, interstellar reddening, and parallax of the standard stars. At each walker step the corrections between the two filter systems are saved. This gives us the ability to propagate the effects of any non-trivial correlations through to the uncertainties in the desired offsets. We run 100 walkers for 10,000 steps and discard the first 2000 as burn-in.

We measure the atmospheric extinction in each filter by fitting a first order polynomial to the instrumental magnitudes as a function of airmass of any bright stars included in an observing run that covers a good airmass range on the same night as our target. We then use this, along with the transformed Super-SDSS standard star magnitudes, to calibrate the comparison star of our target. The target is therefore calibrated by performing differential photometry against this comparison star.

3.3 Comparison with previously published systems

3.3.1 NN Ser

NN Ser is a well-characterised eclipsing binary, first discovered by Haefner (1989), containing a hot WD and an M dwarf companion with more than a decade of archival high-speed multi-colour photometry. Parsons et al. (2010) combined ULTRACAM photometry with phase-resolved UVES spectroscopy to obtain precise parameters for the system, independent of any mass-radius relations. This makes it an ideal system with which to test the purely photometric approach presented in this paper. Additionally NN Ser has been observed with HiPERCAM allowing us to test the method with simultaneous $u_s g_s r_s i_s z_s$ data.

Initial fits to the HiPERCAM photometry struggled, attempting to change the parallax to values inconsistent with the *Gaia* measurement. We determined this was due to the M dwarf SED (the in-eclipse HiPERCAM photometry) not matching the PHOENIX model for the published parameters, instead preferring a higher temperature model. The fit was compensating for this by altering the radius, and therefore mass of the secondary, having an effect on the rest of the system parameters. This likely reflects the fact that the high irradiation experienced by the M dwarf prevents it from being well represented by the PHOENIX models, even on the unirradiated face seen during the primary eclipse. Allowing the temperature of the secondary to be independent in each band solved this issue, allowing the MCMC to converge to a fit consistent with the *Gaia* parallax.

Our best fit to the HiPERCAM photometry (see Table 3 and Figure 2) achieves uncertainties (and therefore precisions) in the WD mass, effective temperature, and secondary mass of 1.8, 4.6, and 5.7 per cent respectively. Although our secondary mass is ≈ 11 per cent more massive than the published value it is still consistent to better than 2σ. The other parameters all lie within 1σ of the high precision, published values (Parsons et al. 2017, 2018). This demonstrates that, even for systems with highly irradiated companions, our method can still be successful.

3.3.2 SDSS J0838+1914

SDSS J0838+1914 (SDSS J083845.86+191416.5 in SIMBAD, also known as CSS 40190) is another well characterised PCEB and was discovered by Drake et al. (2010) in the Catalina Sky Survey. It was later characterised by Parsons et al. (2017, 2018) who found it to contain a WD with a temperature and mass of $14\,900 \pm 730$ K and 0.482 ± 0.008 M$_\odot$, respectively, in a 3.123 h orbit with a 3100 ± 100 K main sequence companion with a mass of 0.142 ± 0.013 M$_\odot$. It is therefore a fairly typical example of a PCEB. Good quality archival ULTRACAM photometry is available for this system. It has also been characterised from SDSS spectroscopy making it a good system with which to compare our photometric fit against the spectroscopic one.

Fitting the ULTRACAM eclipse photometry of the system (see Table 3 and Figure 2) we achieve a precision in the WD mass and effective temperature of 2.9 and 2.4 per cent respectively and the secondary mass and effective temperature of 6.1 and 0.3 per cent respectively. Comparing these to the SDSS spectroscopic values which determine the WD mass and effective temperature to a precision of 9.0 and 3.0 per cent respectively and the secondary mass to 49 per cent demonstrates that we can reach a higher precision using eclipse photometry. Additionally all our best fit values lie within 2σ of the high-precision, published values (Parsons et al. 2017, 2018).

3.3.3 SDSS J1028+0931

SDSS J1028+0931 (SDSS J102857.78+093129.8 in SIMBAD) was discovered to be an eclipsing WDdM system by Parsons et al. (2013). Later and more precise characterisation was performed by Parsons

et al. (2017, 2018), who found a WD temperature and mass of $12\,221 \pm 765$ K and 0.4146 ± 0.0036 $M_\odot$, respectively with the fit to the secondary giving a temperature and mass of $3\,500 \pm 100$ K and 0.403 ± 0.005 $M_\odot$. The higher mass secondary in this system means that the spectrum is dominated by the M dwarf redward of the g band with measurable contribution in the u band. This makes it a difficult system to characterise from low-resolution spectroscopy due to the dilution of the Balmer series of the WD by the M dwarf. We fit this system in order to show that the presence of eclipses overcomes the issues caused by the superposition of both SEDs and results in a more robust fit.

The secondary of SDSS J1028+0931 appears to have at least one significant star spot on its surface which adds an additional slope to the photometry. We add a linear term to the g_s and r_s band models to account for this. The best fit including these two additional parameters (see Table 3 and Figure 2) achieves an precision of 1.4 per cent on the WD mass and 1.9 per cent on its temperature. For the M dwarf we manage 5.3 and 0.8 per cent respectively for the mass and temperature. Again, all of our best-fit parameters are within 2σ of the high-precision values of Parsons et al. (2017, 2018). Comparing our fit with the spectroscopic values from SDSS demonstrates the benefit of eclipse photometry in systems where one component dominates, with the spectroscopic determination of the WD temperature being discrepant by over 4σ and the mass being discrepant by almost 10σ.

3.4 New systems

With the code proving successful for these three well-characterised systems, we now apply it to three previously uncharacterised PCEBs observed with ULTRACAM. Best-fit parameters are listed in Table 4 with the light curves shown in Figure 3.

3.4.1 2MASS J1358−3556

2MASS J1358−3556 (2MASS J13581075−3556194 in the 2MASS catalogue or Gaia DR2 6121651418527918976 in SIMBAD) was found to be an eclipsing PCEB by combining *Gaia* measurements and data from the Catalina Real-Time Transient Survey (CRTS) (Drake et al. 2009). Fitting the ULTRACAM eclipse photometry in u_s, g_s, and i_s gives a WD mass of 0.438 ± 0.007 $M_\odot$ with an effective temperature of $40\,600^{+1600}_{-2200}$ K assuming a helium core composition. Rerunning the fit with a carbon-oxygen core mass-radius relation favours a lower WD mass of 0.38 $M_\odot$. This mass is below what is expected for a WD with a CO-core composition and so the helium fit appears the most consistent. The M dwarf in this system fits best with a mass of 0.118 ± 0.006 $M_\odot$ and an effective temperature of 2980^{+30}_{-40} K. The best fit parameters are shown in Table 4 with the light curve model shown in Figure 3. This system appears to be a fairly typical, if quite young, PCEB due to the high WD temperature.

3.4.2 EC 12250−3026

EC 12250−3026 was initially found in the Edinburgh-Cape blue object survey (Stobie et al. 1997) where it was thought to be a single hot subdwarf. It was later found to be an eclipsing WDdM system in CRTS. The fit to the ULTRACAM photometry (Table 4, Figure 3) gives a WD temperature of $33\,900^{+1000}_{-1300}$ K with a mass of $0.420^{+0.010}_{-0.009}$ $M_\odot$, again favouring a helium core composition. The secondary in this system – which is only detected in the i_s band – is quite low mass at 0.089 ± 0.005 $M_\odot$ although still stellar. The low-mass of the secondary star makes this an interesting system for

investigating the brown dwarf transition regime. For the secondary temperature, we find 2840^{+60}_{-30} K although it is worth mentioning that, like NN Ser, the high temperature of this WD may mean that the best fit temperature of the M dwarf is influenced by the high irradiation and is not necessarily representative of the true unirradiated temperature.

3.4.3 SDSS J1642+0135

SDSS J1642+0135 (SDSS J164251.54+013554.9 in SIMBAD) was discovered by Denisenko & Larin (2018) who determined it to be a pre-cataclysmic variable with a cool ($T_{\rm eff} \lessapprox 8000$ K) white dwarf primary and strong ellipsoidal modulation. This system is of particular interest as its period of 2.31 h places it in the cataclysmic variable (CV) period gap. Initial fits of this system were unable to match the extreme ellipsoidal modulation present in the g_s and i_s band photometry, even with a Roche lobe filling factor equal to one. This required adding the secondary gravity-darkening exponent, β_1 (Claret & Bloemen 2011), to the model as a free parameter, allowing the fit to increase the effect of gravity darkening, preferring a value of $\beta_1 = 0.41 \pm 0.02$. This is roughly twice what would be expected for a star of the best fit temperature (Claret 2003), however, observational validation of how β_1 varies with effective temperature seems to indicate a fairly large scatter around the theoretical values (Claret 2003, see figure 3). With the addition of β_1 as a free parameter we confirm the predictions of Denisenko & Larin (2018), finding a 7650 ± 60 K WD with a mass of $0.69^{+0.010}_{-0.011}$ $M_\odot$ and a secondary that is on the verge of – if not already – filling its Roche lobe with a linear filling factor of 0.97 ± 0.017. We find a secondary mass of 0.198 ± 0.010 $M_\odot$ and effective temperature of 2897^{+5}_{-6} K. The higher than average WD mass for PCEBs (Zorotovic et al. 2011) is consistent with that of the volume-limited CV population (Pala et al. 2020). Additionally, the secondary mass matches the donor mass of $M_{\rm donor} = 0.2 \pm 0.02$ $M_\odot$ at which CV mass transfer ceases at the start of the period gap, as determined by Knigge (2006). It therefore seems possible that SDSS J1642+0135 is a temporarily detached CV in the final stages of crossing the period gap with an orbital period ≈ 10 mins greater than the predicted period at the lower edge of the gap of $P = 2.15$ h (Knigge 2006). A population of apparently gap-crossing CVs has been identified statistically using the SDSS sample of PCEBs (Zorotovic et al. 2016), however, this may be one of the first specific examples of an eclipsing, gap-crossing CV and is worth more detailed study.

4 DISCUSSION

Assessing the precision of our fits to the six systems, the median percentage uncertainty on the WD mass determination is 1.7 per cent with a maximum uncertainty of 2.9 per cent for SDSS J0838+1914. For the secondary mass these median and maximum uncertainties are 5.5 per cent and 6.1 per cent respectively which is dominated by the 5 per cent estimated contribution from systematic errors arising from the intrinsic scatter of the M dwarf mass-radius relationship. This precision is, therefore, at or below the aim of 5 per cent precision which is necessary to discern systems with interesting subtypes of either component. Comparing these percentage uncertainties with the two other methods of characterisation mentioned – spectral decomposition (Rebassa-Mansergas et al. 2012) and VOSA SED fitting (Rebassa-Mansergas et al. 2021) – demonstrates that using the eclipse gives similar or better precision. For the WD mass, the median percentage uncertainty of the SDSS sample (Rebassa-Mansergas et al.
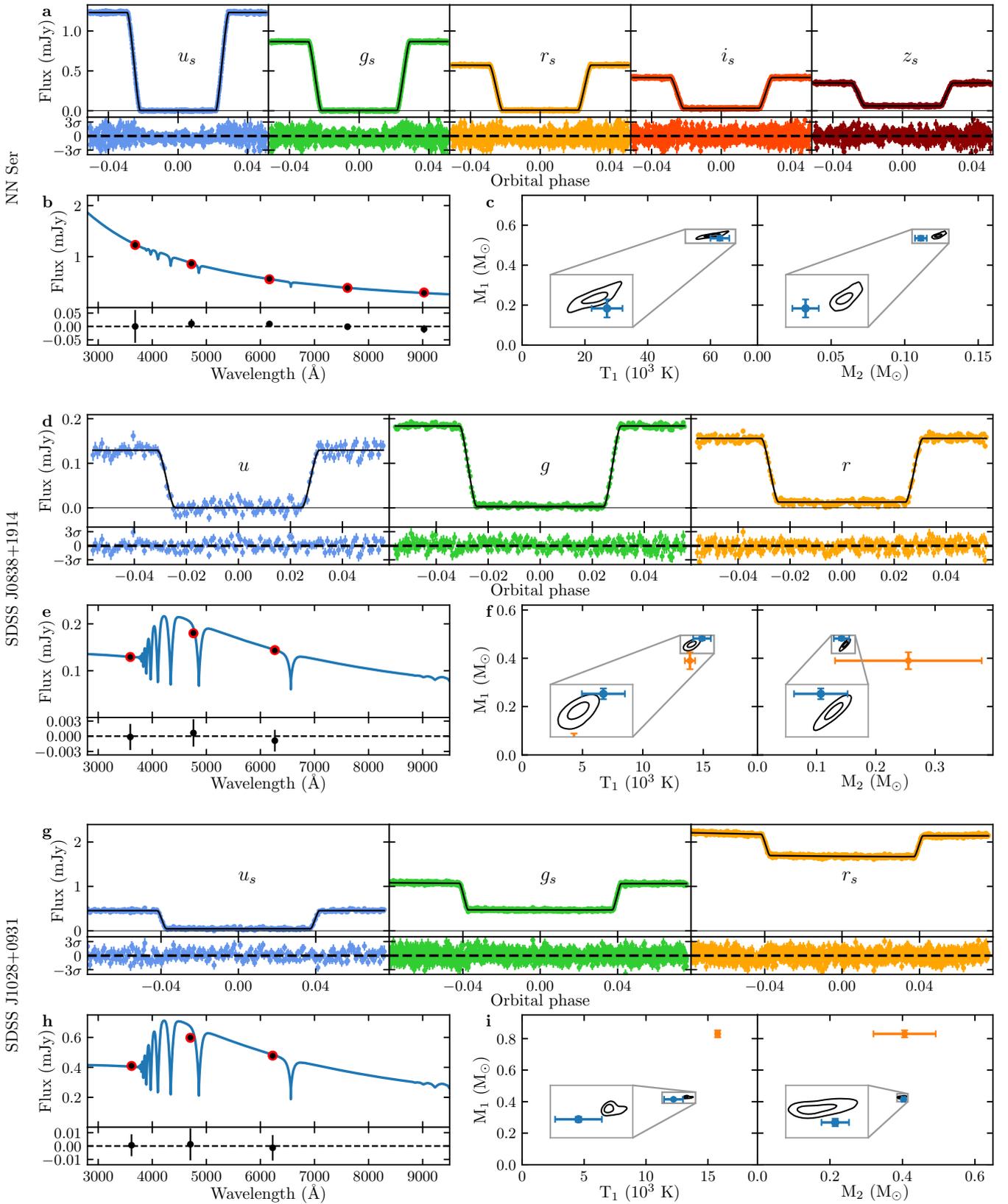
Figure 2. Best fit results for the three previously published systems. Light curve plots show the flux calibrated eclipse light curve data (coloured points) along with the best fit eclipse model (black line). A horizontal black line shows a flux of zero for reference with the residuals shown below. The panel below the light curves to the left shows the SED of the WD i.e. the depths of the eclipses in each band (black points). These are shown against the Koester (2010) model spectrum for the best fit parameters (blue line) and the synthetic photometry from this model (red points) with the residuals below. The panel to the right shows the 1σ and 2σ contours from our MCMC fit along with the published parameters (blue points, Parsons et al. 2017, 2018) and those derived from SDSS spectroscopy where available (orange points, Rebassa-Mansergas et al. 2012).

	NN Ser		SDSS J0838+1914		SDSS J1028+0931	
	μ	Difference %(σ)	μ	Difference %(σ)	μ	Difference %(σ)
T_1(K)	60800^{+2200}_{-2800}	$-3.5(-0.6)$	14060^{+340}_{-340}	$-5.7(-1.0)$	13270^{+250}_{-140}	$+8.6(+1.3)$
T_2(K)	–	–	2910^{+10}_{-10}	$-6.2(-1.9)$	3550^{+30}_{-20}	$+1.3(+0.4)$
M_1(M$_\odot$)	$0.548^{+0.010}_{-0.009}$	$+2.4(+0.9)$	$0.456^{+0.012}_{-0.013}$	$-5.2(-1.7)$	$0.428^{+0.006}_{-0.006}$	$+3.2(+1.9)$
M_2(M$_\odot$)	$0.123^{+0.007}_{-0.007}$	$+10.8(+1.6)$	$0.148^{+0.009}_{-0.009}$	$+4.3(+0.4)$	$0.397^{+0.021}_{-0.021}$	$-1.4(-0.3)$

Table 3. Comparison of parameters determined using our purely photometric method against published, model-independent values (Parsons et al. 2017, 2018). We show the deviation from the published values as a percentage and in units of standard deviation where the standard deviation is the uncertainty from our photometric fit summed in quadrature with the uncertainty of the published value. We also include a 1 per cent and 5 per cent systematic error contribution for the primary and secondary masses respectively.

Target	T_1 (K)	T_2 (K)	M_1 (M$_\odot$)	M_2 (M$_\odot$)	i (°)	$E(B-V)$	T_0 (BMJD)	P (d)
2MASS J1358−3556	40600^{+1600}_{-2200}	2980^{+30}_{-40}	$0.438^{+0.007}_{-0.007}$	$0.118^{+0.006}_{-0.006}$	$88.7^{+0.9}_{-1.3}$	$0.04^{+0.01}_{-0.01}$	58270.1646820(12)	0.0815296700(35)
EC 12250−3026	33900^{+1000}_{-1300}	2840^{+60}_{-30}	$0.420^{+0.010}_{-0.009}$	$0.089^{+0.005}_{-0.005}$	$85.1^{+0.1}_{-0.2}$	$0.04^{+0.01}_{-0.01}$	58269.97928329(67)	0.1234482746(40)
SDSS J1642+0135	7650^{+60}_{-60}	2897^{+5}_{-6}	$0.693^{+0.010}_{-0.011}$	$0.198^{+0.010}_{-0.010}$	$89.1^{+0.6}_{-0.7}$	$0.01^{+0.01}_{-0.01}$	58546.3505016(17)	0.09629068740(52)

Table 4. Results of the MCMC fits to the three new WDdM systems.
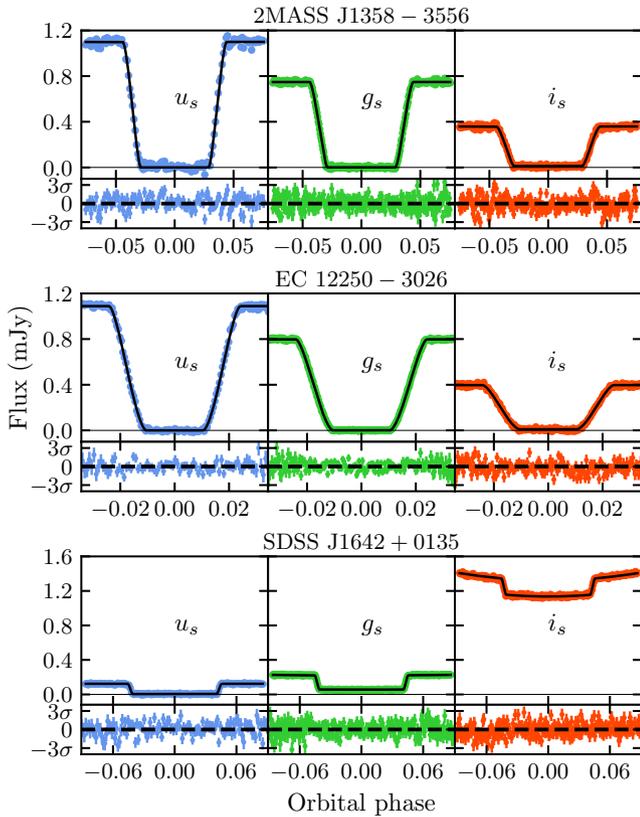
Figure 3. Best fits to ULTRACAM eclipse photometry of the three new systems. The best fit model is shown by the solid black line while a thin black line shows the zero level. Normalised residuals are shown below with a dashed black line showing zero.

2012) is 18 percent with a 16th percentile (comparable to one standard deviation below the mean for non-normal distributions) of 7 per cent. For the VOSA sample (Rebassa-Mansergas et al. 2021) the median is 11 per cent with a 16th percentile of 6 per cent. Our mass determinations are therefore significantly more precise than either of these methods. To illustrate this point further, our least precise

measurement of WD mass is more precise than 98.5 per cent of WD mass measurements in the SDSS sample and better than all WD mass measurements in the VOSA sample. For the WD temperature our uncertainties are much more comparable, with a median uncertainty of 3 per cent and a maximum of 5 per cent. This is compared with a median value of 4 per cent for the SDSS sample.

Comparing our best fit parameters to the published, model-independent values (Table 3) additionally demonstrates that a purely photometric approach relying only on eclipse photometry can yield parameters with greater reliability and accuracy than from low-resolution spectroscopy. This improvement on the spectroscopic method is particularly obvious in SDSS J1028+0931 where the contribution from the M dwarf companion is significant. For all three systems, our parameters are consistent to within 2σ of the published parameters with most values accurate to better than $\approx$ 5 per cent. This level of accuracy is better than the original goal of 3σ.

Possible sources of systematic error that we haven't accounted for include the assumption of thick, DA WD models. Although this is consistent with the findings of Parsons et al. (2017), it will lead to systematic errors if used for a system containing a WD with a thin hydrogen atmosphere or a helium atmosphere. Additionally, many of the systems considered here contain WDs with masses in the range where theorised hybrid WDs lie (Zenati et al. 2019). Although these have not been confirmed observationally, with a tentative suggestion from Parsons et al. (2020) that has been supported by (Romero et al. 2021), a hybrid core would introduce a similar error into the WD parameters due to an incorrect mass-radius relation. For the secondary, the best-fit effective temperature can be affected by the presence of star spots on the surface or from irradiation effects due to a hot WD, as seems to be the case in NN Ser. It is also worth mentioning that the statistical uncertainties on the secondary temperature resulting from the MCMC fit are very likely underestimated. The PHOENIX (Husser et al. 2013) model grid that we use has a 100 K resolution in effective temperature and so any uncertainties much below this level are unlikely to represent the true error.

Given the success of eclipse photometry for initial characterisation of WDdM systems, the method will be applicable to LSST data. How well this works will depend on the quality of the absolute flux calibration as well as the final survey strategy, particularly whether the individual 15 s images or photometry are available. This is due to the need to resolve the sharp eclipse features in order to constrain the radii

(and hence, masses) of the components. As previously mentioned, many systems discovered by LSST will have little to no parallax information initially (LSST will provide parallax measurements to many of these as the survey progresses). Although fitting the eclipse photometry is still possible in this case, it is more difficult to flag when a fit is converging to erroneous values as a result of systematics.

5 CONCLUSIONS

We have demonstrated that – when combined with *Gaia* parallax measurements – high-cadence, multi-colour eclipse photometry can be used to determine masses and temperatures of WDdM binaries more reliably than low-resolution spectroscopy, achieving a precision of better than 5 per cent on the WD parameters and better than 6 per cent for the M dwarf, making future follow up of these systems easier and more robust. The use of the primary eclipse also guarantees that the photometric SEDs are analysed at the same orbital phase, preventing any possible issues that may arise from using the Virtual Observatory SED Analyser to fit the system.

Additionally, as well as being able to be used for fainter systems than spectroscopic methods, the photometric nature of this method is better equipped to find systems of particular interest such as those displaying variability due to magnetic or pulsating WDs; high-mass WDs, from their sharp eclipse features; or systems with brown dwarf companions that would otherwise be washed out in the optical if not for the clear eclipses. The lack of need for ID spectroscopy also makes this method more time efficient, with the high-cadence photometry being reusable for any high precision follow up work (unlike ID spectroscopy which is often not useful beyond the initial identification).

We have used this method to determine parameters for three new PCEBs, determining two to contain hot, helium-core WDs with low mass companions (one of which is near the brown dwarf transition regime), and one to be a possibly detached CV close to coming back into contact.

DATA AVAILABILITY

The data underlying this article will be shared upon reasonable request to the corresponding author.

REFERENCES

Allard F., Homeier D., Freytag B., 2012, in Richards M. T., Hubeny I., eds, IAU Symposium Vol. 282, From Interacting Binaries to Exoplanets: Essential Modeling Tools. pp 235–242, doi:10.1017/S1743921311027438
Altavilla G., et al., 2015, Astronomische Nachrichten, 336, 515
Altavilla G., et al., 2021, MNRAS, 501, 2848
Althaus L. G., García-Berro E., Isern J., Córsico A. H., 2005, A&A, 441, 689
Baraffe I., Homeier D., Allard F., Chabrier G., 2015, A&A, 577, A42
Bellm E. C., et al., 2019, PASP, 131, 018002
Bohlin R. C., Colina L., Finley D. S., 1995, AJ, 110, 1316
Choi J., Dotter A., Conroy C., Cantiello M., Paxton B., Johnson B. D., 2016, ApJ, 823, 102
Claret A., 2000, A&A, 363, 1081
Claret A., 2003, A&A, 406, 623
Claret A., Bloemen S., 2011, A&A, 529, A75
Claret A., Cukanovaite E., Burdge K., Tremblay P. E., Parsons S., Marsh T. R., 2020, A&A, 634, A93
Copperwheat C. M., Marsh T. R., Dhillon V. S., Littlefair S. P., Hickman R., Gänsicke B. T., Southworth J., 2010, MNRAS, 402, 1824
Denisenko D. V., Larin I., 2018, arXiv e-prints, p. arXiv:1807.04574
Dhillon V. S., et al., 2007, MNRAS, 378, 825
Dhillon V. S., et al., 2021, MNRAS, 507, 350
Dotter A., 2016, ApJS, 222, 8
Drake A. J., et al., 2009, ApJ, 696, 870
Drake A. J., et al., 2010, arXiv e-prints, p. arXiv:1009.3048
Fontaine G., Brassard P., Bergeron P., 2001, PASP, 113, 409
Foreman-Mackey D., Hogg D. W., Lang D., Goodman J., 2013, PASP, 125, 306
Fukugita M., Ichikawa T., Gunn J. E., Doi M., Shimasaku K., Schneider D. P., 1996, AJ, 111, 1748
Gaia Collaboration et al., 2016, A&A, 595, A1
Gaia Collaboration et al., 2021, A&A, 649, A1
Graham M. J., et al., 2019, PASP, 131, 078001
Haefner R., 1989, A&A, 213, L15
Han Z., Podsiadlowski P., Maxted P. F. L., Marsh T. R., Ivanova N., 2002, MNRAS, 336, 449
Husser T. O., Wende-von Berg S., Dreizler S., Homeier D., Reiners A., Barman T., Hauschildt P. H., 2013, A&A, 553, A6
Ivezić Ž., et al., 2019, ApJ, 873, 111
Kesseli A. Y., Muirhead P. S., Mann A. W., Mace G., 2018, AJ, 155, 225
Knigge C., 2006, MNRAS, 373, 484
Koester D., 2010, Mem. Soc. Astron. Italiana, 81, 921
López-Morales M., 2007, ApJ, 660, 732
López-Morales M., Ribas I., 2005, ApJ, 631, 1120
Mann A. W., et al., 2019, ApJ, 871, 63
Marinoni S., et al., 2016, MNRAS, 462, 3616
Morrell S., Naylor T., 2019, MNRAS, 489, 2615
Pala A. F., et al., 2020, MNRAS, 494, 3799
Pancino E., et al., 2012, MNRAS, 426, 1767
Pancino E., et al., 2021, MNRAS, 503, 3660
Panei J. A., Althaus L. G., Chen X., Han Z., 2007, MNRAS, 382, 779
Parsons S. G., Marsh T. R., Copperwheat C. M., Dhillon V. S., Littlefair S. P., Gänsicke B. T., Hickman R., 2010, MNRAS, 402, 2591
Parsons S. G., et al., 2013, MNRAS, 429, 256
Parsons S. G., et al., 2015, MNRAS, 449, 2194
Parsons S. G., et al., 2017, MNRAS, 470, 4473
Parsons S. G., et al., 2018, MNRAS, 481, 1083
Parsons S. G., et al., 2020, Nature Astronomy, 4, 690
Rebassa-Mansergas A., Gänsicke B. T., Rodríguez-Gil P., Schreiber M. R., Koester D., 2007, MNRAS, 382, 1377
Rebassa-Mansergas A., Gänsicke B. T., Schreiber M. R., Koester D., Rodríguez-Gil P., 2010, MNRAS, 402, 620
Rebassa-Mansergas A., Nebot Gómez-Morán A., Schreiber M. R., Gänsicke B. T., Schwope A., Gallardo J., Koester D., 2012, MNRAS, 419, 806
Rebassa-Mansergas A., Agurto-Gangas C., Schreiber M. R., Gänsicke B. T., Koester D., 2013, MNRAS, 433, 3398

Rebassa-Mansergas A., Ren J. J., Parsons S. G., Gänsicke B. T., Schreiber M. R., García-Berro E., Liu X. W., Koester D., 2016, MNRAS, 458, 3808

Rebassa-Mansergas A., et al., 2021, MNRAS, 506, 5201

Ritter H., Zhang Z. Y., Kolb U., 2000, A&A, 360, 959

Romero A. D., Lauffer G. R., Istrate A. G., Parsons S. G., 2021, MNRAS,

Smith J. A., et al., 2002, AJ, 123, 2121

Stobie R. S., et al., 1997, MNRAS, 287, 848

Toonen S., Nelemans G., 2013, A&A, 557, A87

Van Roestel J., 2019, in Tovmassian G. H., Gansicke B. T., eds, Compact White Dwarf Binaries. p. 17

Wild J. F., et al., 2021, MNRAS,

Willems B., Kolb U., 2004, A&A, 419, 1057

Zenati Y., Toonen S., Perets H. B., 2019, MNRAS, 482, 1135

Zorotovic M., Schreiber M. R., Gänsicke B. T., Nebot Gómez-Morán A., 2010, A&A, 520, A86

Zorotovic M., Schreiber M. R., Gänsicke B. T., 2011, A&A, 536, A42

Zorotovic M., et al., 2016, MNRAS, 457, 3867

APPENDIX A: HIPERCAM PHOTOMETRIC SYSTEM

As previously mentioned, while the HiPERCAM photometric system approximates the SDSS system (Figure A1), there are some departures, most significantly in the u_s band where the difference is on the order of a few tenths of magnitudes. To assess any colour terms we follow the procedure of Wild et al. (2021), using synthetic photometry of main sequence stars and WDs to provide corrections as a function of SDSS colour.

For main sequence stars we use PHOENIX spectral models (Allard et al. 2012) at effective temperatures and surface gravities defined by a MIST (Dotter 2016; Choi et al. 2016) isochrone with an age = $10^{8.5}$ yr, covering masses ranging from $0.1 - 3 \, \mathrm{M_\odot}$ and surface gravities from $3.7 - 4.7$. For WDs we use Koester (2010) models with a $\log(g \, [\mathrm{cgs}]) = 8.5$ over the full range of available model temperatures. We then use Equation 2 to generate synthetic photometry for the HiPERCAM Super-SDSS and SDSS systems. Corrections as a function of colour are shown in Figure A2 with best fit colour terms shown in Tables A1 and A2 for WDs and main sequence stars respectively. Corrections should be possible to an accuracy of a couple of per cent in the g_s, r_s, i_s, and z_s bands using main sequence stars but it is clear that no easy correction can be made for u_s where there is no consistent correlation with colour. As such, any correction to the u_s band magnitudes using main sequence stars in combination with these colour terms should be avoided if possible. Using WDs make this a lot easier with tight relations between the colour and corrections that only weakly depend on the surface gravity of the WD (as demonstrated by the similarity of $\log(g) = 8.0$ and $\log(g) = 8.5$ relations).

In order to make flux calibration simpler and more robust in future, we define a set of HiPERCAM standard stars (Table A3). These standard stars are the *Gaia* spectro-photometric standard stars collated and evaluated by Pancino et al. (2012); Altavilla et al. (2015); Marinoni et al. (2016); Altavilla et al. (2021); Pancino et al. (2021) who provide high quality spectra of these standards covering the full range of the HiPERCAM photometric system. We again use Equation 2 to produce synthetic AB magnitudes for these stars in both the HiPERCAM and ULTRACAM systems. Pancino et al. (2021) mentions that the scatter in the spectro-photometric standard stars when compared with literature is of order 1 per cent with discrepant behavior of a similar order in the red for faint blue stars. Additionally, due to the use of spectral models to extend the flux tables below 400 nm and above 800 nm, we estimate an uncertainty of 2 per cent in u_s and z_s, and 1 per cent in g_s, r_s, and i_s.
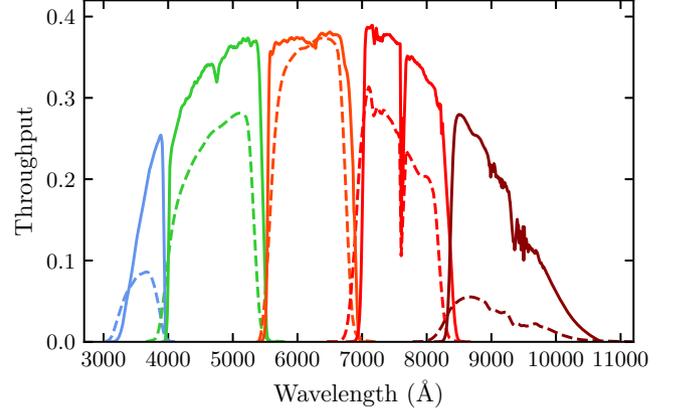
Figure A1. Filter profiles plotted for both HiPERCAM Super-SDSS ($u_s g_s r_s i_s z_s$) (Dhillon et al. 2021) and SDSS ($u'g'r'i'z'$) (Fukugita et al. 1996) photometric systems, both including the instrument, telescope, and atmosphere. Solid lines indicate the HiPERCAM system while dashed lines show the SDSS system.

Table A1. SDSS to HiPERCAM Super-SDSS colour terms for WDs. Validity shows the range of colours spanned by the models that the colour terms were fit to. These take the form of a straight line, e.g. $u_s - u' = -0.211(g'-r') - 0.038$

Correction	Gradient	Variable	y-intercept	Validity
$u_s - u'$	−0.211	$g' - r'$	−0.038	$-0.55 < g' - r' \le 0.20$
	−0.438	$g' - r'$	0.006	$0.20 < g' - r' \le 0.70$
$g_s - g'$	−0.047	$g' - r'$	−0.009	$-0.55 < g' - r' \le 0.70$
$r_s - r'$	−	−	−	−
$i_s - i'$	−0.093	$r' - i'$	0.005	$-0.40 < r' - i' \le 0.25$
$z_s - z'$	−0.047	$i' - z'$	−0.009	$-0.35 < i' - z' \le 0.10$

Table A2. As Table A1 but for main sequence models.

Correction	Gradient	Variable	y-intercept	Validity
$u_s - u'$	0.120	$g' - r'$	−0.257	$0.00 < g' - r' \le 1.30$
$g_s - g'$	−0.047	$g' - r'$	−0.009	$-0.25 < g' - r' \le 1.30$
$r_s - r'$	-0.004	$g' - r'$	0.000	$-0.25 < g' - r' \le 1.30$
$i_s - i'$	−0.093	$r' - i'$	0.005	$-0.25 < g' - r' \le 0.55$
$z_s - z'$	0.000	$i' - z'$	0.000	$-0.20 < i' - z' \le 0.10$
	−0.047	$i' - z'$	−0.009	$0.10 < i' - z' \le 0.30$
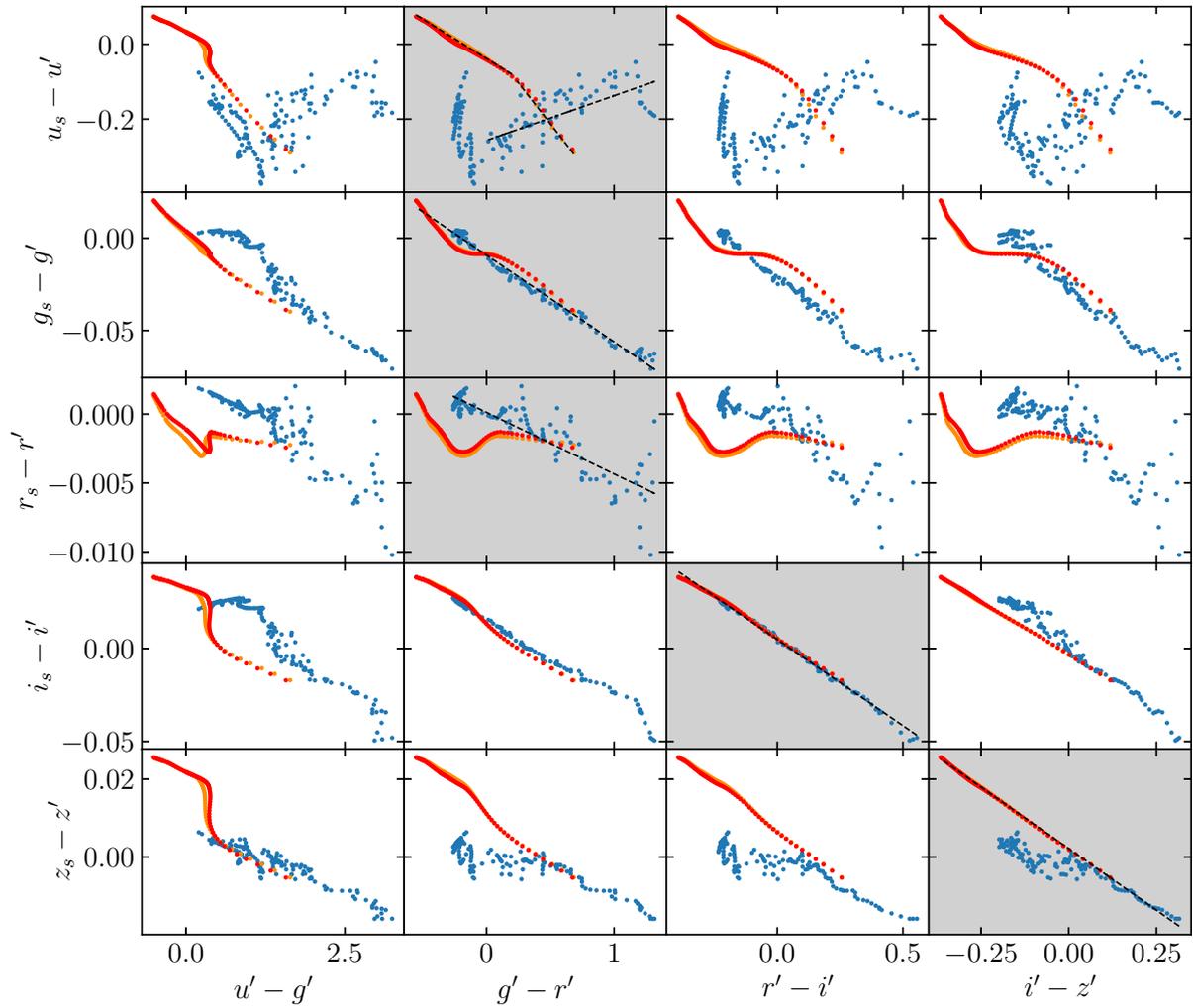
Figure A2. Magnitude offsets between the HiPERCAM Super-SDSS ($u_s g_s r_s i_s z_s$) photometric system (Dhillon et al. 2021) and the SDSS primed ($u'g'r'i'z'$) photometric system (Fukugita et al. 1996) as a function of SDSS colour for main sequence stars (Allard et al. 2012) (blue) with age = $10^{8.5}$ yr and for WDs (Koester 2010) with a $\log(g) = 8.0$ (red) and $\log(g) = 8.5$ (orange). Shaded plots indicate relations to which colour terms are fit and these best fit corrections (listed in Tables A1 and A2) are shown by a black dashed line.

Table A3. *Gaia* spectro-photometric standard stars (Pancino et al. 2012; Altavilla et al. 2015; Marinoni et al. 2016; Altavilla et al. 2021; Pancino et al. 2021) with AB magnitudes computed for the HiPERCAM and ULTRACAM Super-SDSS ($u_s g_s r_s i_s z_s$) photometric systems using the flux tables of Pancino et al. (2021). The 'Type' column indicates the status of a flux standard as either 'Pillar', 'Primary', or 'Secondary' as described in Pancino et al. (2012) ('0', '1', and '2' respectively in the table). The pillars denoted here are the same three stars on which the CALSPEC system is based (Bohlin et al. 1995) and the primary stars are all bright, well-known spectro-photometric standards that are already tied to – or are easy to tie to – the CALSPEC flux scale. Secondary standards are then calibrated from these primary stars. The 'Stability' column shows which standards have been confirmed as photometrically constant by the variability monitoring campaign (Marinoni et al. 2016). Standards that are not yet confirmed as photometrically constant are still considered likely to be constant (Marinoni et al. 2016, see section 3.4). We therefore choose not to discard them.

Name	RA (J2000)	DEC (J2000)	HiPERCAM					ULTRACAM					Type	SpType	Stability
			u_s	g_s	r_s	i_s	z_s	u_s	g_s	r_s	i_s	z_s			
WD 0004+330	00:07:32.26	+33:17:27.60	13.158	13.531	14.023	14.426	14.742	13.125	13.523	14.042	14.424	14.781	2	DA1	
WD 0018−267	00:21:30.73	−26:26:11.46	15.252	14.083	13.621	13.431	13.391	15.302	14.094	13.610	13.433	13.385	2	DA9	
WD 0038+555	00:41:21.99	+55:50:08.40	14.014	13.980	14.106	14.280	14.442	14.019	13.980	14.113	14.280	14.471	2	DQ5	Confirmed
LTT 377	00:41:30.47	−33:37:32.03	13.783	11.279	9.973	9.275	9.060	13.889	11.296	9.948	9.283	9.062	2	K9	Confirmed
WD 0046+051	00:49:09.90	+05:23:19.01	13.578	12.556	12.301	12.268	12.395	13.574	12.567	12.298	12.268	12.407	2	DZ7	Confirmed
WD 0047−524	00:50:03.68	−52:08:15.60	14.172	14.059	14.422	14.741	15.036	14.171	14.054	14.439	14.738	15.069	2	DA2	
WD 0050−332	00:53:17.44	−32:59:56.60	12.767	13.095	13.589	13.934	14.191	12.742	13.086	13.607	13.932	14.222	2	DA1	
WD 0109−264	01:12:11.65	−26:13:27.69	12.695	12.883	13.355	13.724	14.025	12.691	12.875	13.372	13.722	14.058	2	DA1	
WD 0123−262	01:25:24.45	−26:00:43.90	15.531	15.144	15.008	15.013	15.130	15.580	15.149	15.006	15.013	15.145	2	DC	Confirmed
G245-31	01:38:39.39	+69:38:01.50	15.886	14.849	14.243	13.983	13.865	15.953	14.860	14.228	13.985	13.865	2	K	Confirmed
GJ 70	01:43:20.18	+04:19:17.97	13.931	11.815	10.445	9.286	8.799	14.173	11.834	10.416	9.297	8.761	2	M2	Confirmed
LTT 1020	01:54:50.27	−27:28:35.74	12.542	11.736	11.361	11.226	11.215	12.614	11.745	11.353	11.227	11.216	1	G	Confirmed
LP 885-23	02:07:06.33	−30:24:22.90	17.474	14.894	13.549	12.138	11.558	17.620	14.914	13.515	12.152	11.516	2	M0	Confirmed
EGGR 21	03:10:31.02	−68:36:03.39	11.468	11.258	11.563	11.855	12.151	11.467	11.254	11.578	11.851	12.179	1	DA3	Confirmed
HG 7-15	03:48:11.86	07:08:46.47	14.059	11.513	10.274	9.710	9.426	14.134	11.528	10.250	9.716	9.409	2	M1	Confirmed
LTT 1788	03:48:22.67	−39:08:37.20	14.013	13.327	13.025	12.907	12.902	14.098	13.334	13.018	12.909	12.908	1	F	Confirmed
GD 50	03:48:50.20	−00:58:31.20	13.401	13.797	14.290	14.683	15.040	13.367	13.788	14.308	14.681	15.081	1	DA2	
HZ 2	04:12:43.55	+11:51:49.00	13.719	13.709	14.076	14.410	14.688	13.706	13.703	14.092	14.407	14.714	1	DA3	
WD 0455−282	04:57:13.90	−28:07:54.00	13.262	13.649	14.181	14.581	14.887	13.237	13.640	14.199	14.578	14.930	2	DA1	
WD 0501−289	05:03:55.51	−28:54:34.57	13.086	13.583	14.122	14.559	14.899	13.057	13.572	14.141	14.557	14.936	2	DO	Confirmed
G191-B2B	05:05:30.61	+52:49:51.95	11.069	11.492	12.010	12.427	12.778	11.031	11.483	12.029	12.423	12.813	0	DA0	Confirmed
GD 71	05:52:27.63	+15:53:13.37	12.480	12.783	13.258	13.654	14.000	12.451	12.775	13.277	13.651	14.034	0	DA1	Confirmed
LTT 2415	05:56:24.74	−27:51:32.35	13.045	12.348	12.115	12.032	12.041	13.156	12.354	12.110	12.033	12.053	1	G	Confirmed
HD 270477	05:59:33.36	−67:01:13.72	11.392	10.501	10.316	10.306	10.354	11.528	10.506	10.314	10.306	10.363	2	F8	
HD 271747	05:59:58.62	−66:06:08.91	12.824	11.689	11.303	11.194	11.196	12.904	11.699	11.294	11.195	11.200	2	G0	
HD 271759	06:00:41.34	−66:03:14.03	11.803	10.862	10.877	10.991	11.090	12.011	10.863	10.881	10.990	11.100	2	A2	Confirmed
HD 271783	06:02:11.36	−66:34:59.13	13.209	12.148	11.783	11.697	11.755	13.310	12.157	11.775	11.698	11.761	2	F5	
WD 0604−203	06:06:13.39	−20:21:07.20	11.773	11.831	12.269	12.608	12.903	11.788	11.825	12.285	12.605	12.937	2	DA	Confirmed
WD 0621−376	06:23:12.63	−37:41:28.01	11.372	11.792	12.325	12.741	13.069	11.341	11.783	12.343	12.738	13.111	2	DA1	Confirmed
HILT 600	06:45:13.37	+02:08:14.70	10.751	10.458	10.452	10.535	10.631	10.820	10.458	10.455	10.535	10.651	1	B1	Confirmed
WD 0644+375	06:47:37.99	+37:30:57.07	11.832	11.882	12.258	12.606	12.906	11.814	11.876	12.275	12.603	12.944	2	DA2	
WD 0646−253	06:48:56.09	−25:23:47.00	13.220	13.419	13.863	14.247	14.507	13.199	13.411	13.881	14.244	14.532	2	DA2	Confirmed
G193-26	07:03:26.29	+54:52:06.00	13.955	13.223	12.812	12.635	12.567	14.019	13.232	12.802	12.637	12.575	2	G	Confirmed
WD 0721−276	07:23:20.10	−27:47:21.60	13.973	14.297	14.771	15.149	15.470	13.949	14.288	14.788	15.145	15.511	2	DA1	Confirmed
LTT 3218	08:41:32.56	−32:56:34.90	12.248	11.875	11.903	12.025	12.186	12.274	11.876	11.908	12.023	12.203	1	DA	Confirmed
G114-25	08:59:03.37	−06:23:46.19	12.976	12.169	11.741	11.551	11.519	13.050	12.179	11.730	11.552	11.524	2	F7	Confirmed
WD 0859−039	09:02:17.30	−04:06:55.45	12.859	12.986	13.385	13.739	14.055	12.841	12.979	13.401	13.736	14.096	2	DA2	Confirmed
GD 108	10:00:47.37	−07:33:30.50	13.195	13.337	13.756	14.101	14.393	13.198	13.328	13.772	14.099	14.431	1	B	Confirmed
LTT 3864	10:32:13.60	−35:37:41.80	13.140	12.358	12.034	11.914	11.902	13.229	12.366	12.027	11.915	11.898	1	F	Confirmed
WD 1031−114	10:33:42.76	−11:41:38.35	12.638	12.808	13.220	13.569	13.871	12.619	12.801	13.236	13.566	13.910	2	DA2	Confirmed
WD 1034+001	10:37:03.81	−00:08:19.30	12.451	12.638	12.925	13.470	14.246	12.416	12.916	13.490	13.901	14.288	2	DOZ1	Confirmed
Feige 34	10:39:36.74	+43:06:09.25	10.451	10.880	11.393	11.781	12.108	10.420	10.871	11.411	11.777	12.152	1	DO	Confirmed
WD 1105−048	11:07:59.95	−05:09:25.90	13.197	12.957	13.245	13.544	13.814	13.193	12.953	13.260	13.541	13.850	2	DA3	Confirmed
SDSS J1138+5729	11:38:02.62	+57:29:23.89	15.855	15.089	14.989	15.010	15.068	16.003	15.093	14.989	15.011	15.082	2	A0/F3	Confirmed

Characterisation of eclipsing WDdM binaries 13

Table A3 – *continued*

Name	RA (J2000)	DEC (J2000)	HiPERCAM					ULTRACAM					Type	SpType	Stability
			u_s	g_s	r_s	i_s	z_s	u_s	g_s	r_s	i_s	z_s			
LTT 4364	11:45:42.92	−64:50:29.46	11.745	11.516	11.477	11.557	11.688	11.778	11.518	11.479	11.556	11.709	1	DQ6	Confirmed
Feige 56	12:06:47.23	+11:40:12.64	11.068	10.872	11.193	11.496	11.713	11.179	10.867	11.207	11.494	11.741	1	B5p	Confirmed
HD 106355	12:14:10.53	−17:14:20.19	12.822	10.641	9.738	9.355	9.146	12.858	10.660	9.716	9.358	9.119	2	G8IV	Confirmed
Feige 66	12:37:23.52	+25:03:59.87	9.924	10.236	10.731	11.138	11.464	9.901	10.228	10.750	11.134	11.505	1	O	Confirmed
SA 104-428	12:41:41.28	−00:26:26.20	15.035	13.088	12.342	12.061	11.914	15.087	13.105	12.324	12.063	11.911	2	G8	Confirmed
SA 104-490	12:44:33.46	−00:25:51.70	13.799	12.779	12.448	12.366	12.367	13.902	12.788	12.441	12.367	12.378	2	G3	Confirmed
GD 153	12:57:02.33	+22:01:52.52	12.723	13.081	13.575	13.986	14.326	12.692	13.072	13.594	13.984	14.361	0	DA1	Confirmed
G14-24	13:02:01.58	−02:05:21.42	14.208	13.148	12.584	12.337	12.224	14.275	13.160	12.570	12.339	12.226	2	K0	Confirmed
GJ 2097	13:07:04.31	+20:48:38.54	15.809	13.219	11.850	10.787	10.313	15.946	13.237	11.822	10.797	10.289	2	M1	Confirmed
HZ 44	13:23:35.26	+36:07:59.51	10.999	11.389	11.885	12.310	12.653	10.971	11.382	11.904	12.307	12.685	1	O	Confirmed
SA 105-663	13:37:30.34	−00:13:17.37	9.755	8.856	8.730	8.706	8.795	9.929	8.861	8.729	8.708	8.799	1	F2	Confirmed
GJ 521	13:39:24.10	+46:11:11.37	13.354	10.933	9.673	8.743	8.320	13.520	10.948	9.645	8.752	8.301	2	M2	Confirmed
HD 121968	13:58:51.17	−02:54:52.32	9.924	10.041	10.423	10.754	11.023	9.950	10.034	10.437	10.752	11.052	1	B1	Confirmed
WD 1408+323	14:10:26.95	+32:08:36.10	13.924	13.833	14.169	14.493	14.790	13.912	13.828	14.185	14.491	14.827	2	DA3	
SDSS J1429+3928	14:29:51.06	+39:28:25.43	15.865	15.006	15.042	15.150	15.233	16.082	15.007	15.047	15.151	15.247	2	A0	Confirmed
G15-10	15:09:46.02	−04:45:06.61	13.170	12.310	11.816	11.608	11.548	13.232	12.320	11.803	11.610	11.548	2	G2	Confirmed
WD 1509+322	15:11:27.66	+32:04:17.80	14.267	14.009	14.276	14.567	14.825	14.265	14.005	14.292	14.565	14.860	2	DA3	Confirmed
2MASS J1517+0202	15:17:38.64	+02:02:25.60	16.234	14.558	13.813	13.474	13.313	16.328	14.575	13.795	13.478	13.308	2		Confirmed
G167-50	15:35:31.55	+27:51:02.20	14.780	13.824	13.305	13.090	13.014	14.829	13.834	13.294	13.092	13.016	2	G	Confirmed
SA 107-544	15:36:48.10	−00:15:07.11	10.163	9.152	8.973	8.945	8.987	10.339	9.157	8.970	8.946	8.986	1	F3	Confirmed
LTT 6248	15:38:59.66	−28:35:36.87	12.720	11.993	11.659	11.526	11.512	12.817	11.999	11.651	11.527	11.523	1	A	Confirmed
G179-54	15:46:08.25	+39:14:16.40	14.612	13.761	13.322	13.148	13.088	14.668	13.771	13.312	13.150	13.094	2	F	Confirmed
G224-83	15:46:14.68	+62:26:39.60	13.777	12.984	12.563	12.391	12.333	13.838	12.993	12.553	12.393	12.339	2	K	Confirmed
G16-20	15:58:18.62	+02:03:06.11	11.966	11.042	10.615	10.441	10.373	12.069	11.051	10.605	10.442	10.380	2	K	Confirmed
GSPC P177-D	15:59:13.57	+47:36:41.90	14.936	13.723	13.279	13.133	13.116	14.991	13.734	13.270	13.135	13.113	1	G0	Confirmed
WD 1606+422	16:08:22.20	+42:05:43.20	14.163	13.758	13.959	14.201	14.435	14.173	13.756	13.972	14.200	14.465	2	DA4	Confirmed
WD 1615−154	16:17:55.26	−15:35:51.90	12.919	13.198	13.649	14.002	14.285	12.896	13.189	13.666	13.999	14.329	2	DA2	
EGGR 274	16:23:33.84	−39:13:46.16	10.712	10.810	11.237	11.583	11.883	10.699	10.804	11.255	11.580	11.922	1	DA2	
G180-58	16:28:16.87	+44:40:38.28	12.554	11.601	11.096	10.889	10.804	12.611	11.612	11.085	10.891	10.808	2	G/K	Confirmed
WD 1626+368	16:28:25.03	+36:46:15.40	14.028	13.805	13.856	13.995	14.168	13.993	13.808	13.862	13.994	14.193	2	DZA6	Confirmed
G170-47	17:32:41.63	+23:44:11.64	10.090	9.191	8.728	8.529	8.457	10.198	9.201	8.717	8.530	8.459	2	G0	Confirmed
2MASS J17430+6655	17:43:04.48	+66:55:01.60	14.495	13.558	13.531	13.605	13.665	14.698	13.560	13.535	13.605	13.670	1	A5	Confirmed
RMC2005 KF08T3	17:55:16.23	+66:10:11.70	15.568	13.731	13.006	12.738	12.605	15.601	13.747	12.989	12.740	12.594	1	K0	Confirmed
TYC 4212-455-1	17:57:13.25	+67:03:40.90	12.811	11.842	11.816	11.905	11.970	13.022	11.845	11.819	11.905	11.979	2	A3	Confirmed
RMC2005 KF06T2	17:58:37.99	+66:46:52.20	16.856	14.518	13.602	13.233	13.038	16.930	14.538	13.579	13.237	13.020	1	K1	Confirmed
BD+66 1071	18:02:10.92	+66:12:26.39	11.579	10.688	10.475	10.449	10.479	11.700	10.694	10.472	10.450	10.489	2	F5	Confirmed
TYC 4209-1396-1	18:05:29.28	+64:27:52.00	13.127	12.238	12.372	12.536	12.649	13.358	12.236	12.380	12.535	12.654	1	A6	Confirmed
TYC 4205-1677-1	18:12:09.57	+63:29:42.30	12.715	11.731	11.781	11.911	12.005	12.929	11.733	11.787	11.911	12.010	1	A5	Confirmed
LTT 7379	18:36:25.95	−44:18:36.94	11.488	10.472	10.077	9.924	9.943	11.560	10.482	10.069	9.925	9.955	1	G0	Confirmed
G184-17	18:40:29.27	+19:36:06.65	15.621	14.453	13.845	13.607	13.490	15.661	14.466	13.832	13.609	13.482	2	K	Confirmed
WD 1845+019	18:47:39.08	+01:57:35.62	12.513	12.726	13.156	13.396	13.418	12.489	12.719	13.173	13.395	13.426	2	DA2	
GJ 745A	19:07:05.56	+20:53:16.97	14.176	11.573	10.171	9.093	8.575	14.315	11.591	10.145	9.104	8.544	2	M2	Confirmed
GJ 745B	19:07:13.20	+20:52:37.24	14.177	11.570	10.173	9.080	8.562	14.311	11.589	10.146	9.092	8.531	2	M2	Confirmed
WD 1914−598	19:18:44.84	−59:46:33.80	14.292	14.219	14.582	14.888	15.203	14.284	14.213	14.598	14.885	15.235	2	DA	Confirmed
EGGR 131	19:20:34.93	−07:40:00.05	12.228	12.219	12.359	12.544	12.750	12.236	12.218	12.366	12.544	12.779	1	DBQA5	Confirmed
WD 1919+145	19:21:40.40	+14:40:43.00	13.128	12.881	13.159	13.469	13.753	13.123	12.877	13.175	13.467	13.782	2	DA3	Confirmed
G23-14	19:51:49.61	+05:36:45.84	12.159	11.059	10.500	10.268	10.164	12.242	11.071	10.487	10.270	10.161	2	G5	Confirmed
WD 2004−605	20:09:05.24	−60:25:41.60	12.721	13.086	13.594	13.972	14.326	12.695	13.077	13.612	13.970	14.363	2	DA1	Confirmed
LTT 7987	20:10:56.85	−30:13:06.64	12.390	12.126	12.420	12.699	12.979	12.389	12.122	12.435	12.696	13.011	1	DA4	Confirmed

Table A3 – *continued*

Name	RA (J2000)	DEC (J2000)	HiPERCAM u_s	g_s	r_s	i_s	z_s	ULTRACAM u_s	g_s	r_s	i_s	z_s	Type	SpType	Stability
WD 2032+248	20:34:21.88	+25:03:49.72	11.348	11.346	11.721	12.078	12.388	11.332	11.340	11.739	12.075	12.421	2	DA2	
WD 2034−532	20:38:16.84	−53:04:25.40	14.089	14.214	14.522	14.783	15.018	14.083	14.212	14.535	14.781	15.045	2	DB4	Confirmed
G24-25	20:40:16.10	+00:33:19.74	11.677	10.806	10.406	10.266	10.216	11.756	10.815	10.398	10.268	10.212	2	G0	Confirmed
WD 2039−682	20:44:21.47	−68:05:21.30	13.354	13.202	13.496	13.776	14.071	13.342	13.198	13.511	13.773	14.101	2	DA3	Confirmed
WD 2047+372	20:49:06.69	+37:28:13.90	13.221	12.918	13.160	13.430	13.693	13.221	12.915	13.175	13.428	13.726	2	DA3	Confirmed
WD 2111+498	21:12:44.05	+50:06:17.80	12.463	12.792	13.270	13.662	13.994	12.435	12.783	13.289	13.659	14.030	2	DA1	
WD 2105−820	21:13:13.90	−81:49:04.00	13.999	13.660	13.734	13.883	14.061	14.004	13.659	13.741	13.880	14.084	2	DA5	Confirmed
WD 2117+539	21:18:56.27	+54:12:41.25	12.530	12.249	12.526	12.828	13.097	12.532	12.245	12.541	12.825	13.123	2	DA3	Confirmed
WD 2134+218	21:36:36.30	+22:04:33.00	14.454	14.329	14.650	14.966	15.232	14.442	14.324	14.666	14.964	15.265	2	DA3	
WD 2140+207	21:42:41.00	+20:59:58.24	13.425	13.245	13.250	13.354	13.480	13.445	13.247	13.253	13.354	13.499	2	DQ6	Confirmed
G93-48	21:52:25.38	+02:23:19.56	12.749	12.622	12.950	13.259	13.552	12.741	12.618	12.966	13.258	13.589	1	DA3	
WD 2216−657	22:19:48.35	−65:29:18.11	14.633	14.484	14.589	14.742	14.920	14.606	14.485	14.596	14.740	14.940	2	DZ5	Confirmed
LTT 9239	22:52:41.03	−20:35:32.89	13.228	12.325	11.905	11.725	11.729	13.292	12.335	11.895	11.726	11.734	1	F	Confirmed
WD 2251−634	22:55:10.00	−63:10:27.00	14.046	13.968	14.328	14.614	14.901	14.041	13.963	14.343	14.612	14.938	2	DA	Confirmed
WD 2309+105	23:12:21.62	+10:47:04.25	12.395	12.812	13.323	13.733	14.079	12.356	12.803	13.342	13.731	14.122	2	DA1	
Feige 110	23:19:58.40	−05:09:56.21	11.168	11.547	12.059	12.446	12.787	11.140	11.539	12.077	12.443	12.821	1	O	Confirmed
WD 2329+407	23:31:35.65	+41:01:30.70	13.953	13.744	14.040	14.347	14.623	13.948	13.739	14.056	14.345	14.657	2	DA3	
WD 2331−475	23:34:02.20	−47:14:26.50	12.760	13.149	13.662	14.042	14.317	12.730	13.140	13.680	14.039	14.345	2	DA1	
WD 2352+401	23:54:56.25	+40:27:30.10	15.229	14.990	14.917	14.977	15.110	15.260	14.992	14.917	14.977	15.137	2	DQ6	Confirmed

This paper has been typeset from a TEX/LATEX file prepared by the author.